Chapter 2

Wetting Properties at Nanometer Scale

Antoniu Moldovan and Marius Enachescu

Additional information is available at the end of the chapter

http://dx.doi.org/10.5772/60886

Abstract

The proposed chapter reviews a series of experimental techniques which enable the accurate quantitative study of wetting properties. The introductive part presents some of the many phenomena and processes influenced by wetting, underlining the importance of understanding the fundamental science involved. A few historical considerations about the quantitative study of wetting and related phenomena are given. Next, some of the "classical" techniques employed for studies at the macroscopic scale are presented. The importance of studies of such phenomena at micro- and nanometer level is underlined, as a consequence of the enormous influence that micro- and nanodevices play in our day to day activities, and examples of quantitative studies, involving various measurement techniques, are given from literature. A description of the basic phenomena related to polarization forces in Scanning Polarization Force Microscopy (SPFM) technique is given, followed by experimental details concerning the actual implementation of the technique. Examples of applications of SPFM are given from literature (from the spreading of liquid crystals on solid substrates to studies of corrosion at nanometer level). Particularly, it is emphasized how this versatile technique was successfully used for direct measurements of contact angles for liquid micro- and nano-droplets, enabling the calculation of the dependence of surface potential energy between the surfaces, the spreading coefficient and the disjoining pressure for micro- and nano-droplets.

Keywords: wetting, contact angle, surface potential energy, disjoining pressure, micro- and nano-droplets, scanning polarization force microscopy

1. Introduction

Wetting, capillarity and adhesion phenomena are so common in our daily lives that most of them go unnoticed. Every painted object is a result of wetting; the oleophobic screens of our smartphones and tablets are a result of wetting-related technology [1]; the integrated circuits that are everywhere have been exposed during fabrication to several steps of wetting processes; the oil inside the engines of our cars wets the moving parts and keeps them running; fruits have natural waxes on their surface to protect them from over- or dehydration [2], etc. Understanding these phenomena and the physical quantities that are involved is extremely important if we want to enhance the desired effects and diminish or eliminate the undesired effects [3,4].

Wetting, capillarity, and adhesion have been subjects of systematic study for at least the last two centuries, the Young's equation being formulated at the beginning of the 19th century. However, basic studies of capillarity, adhesion, and wetting can be traced back to antiquity: Hero of Alexandria (10–70 AD) studied liquids and surface tension, and described in his book "Pneumatics" a series of inventions based on capillary effects, and Pliny the Elder (23–79 AD) wrote in his studies about his interpretation related to the glassy wakes of ships. During the Renaissance, Leonardo da Vinci (1452–1519) analyzed capillarity and envisioned that capillary networks fed mountain water streams. In the 18th century, Benjamin Franklin (1706–1790) was investigating the ability of oil in suppressing waves. Bridging two centuries, Pierre-Simon de Laplace (1749–1827) introduced the term Laplace pressure by investigating the concept of meniscus and offering a theoretical description of the meniscus. A younger polymath but almost during the same period, Thomas Young (1773–1829) described the wetting of solids by fluids [5].

In technology, the implementation of many real-life applications is based on effects related to surface tension, e.g., lab-on-a-chip technology [6], inkjet printing [7], and superhydrophobic surfaces [1]. In biology, surface tension is involved in many basic functions, such as weight support and propulsion at the water surface [5], in natural strategies for water-repellency [2], in the functioning of lungs [8,9], etc. The dynamics of raindrops, groundwater flows, oil spill dynamics, chemical leaching, the water-repellency of soils, and disease transmission via droplet exhalation represent a few of the surface-tension-related phenomena and applications in geophysics and environmental science [5].

2. Techniques for surface energy and wetting investigation from macro- to nanoscale

Most of the techniques involved in the determination of wetting properties are based on measurements of the contact angle. The contact angle is a convenient parameter which describes the ability of a liquid to wet a surface in a gaseous environment, and it is related to the interfacial energies by the well-known Young's equation:

http://dx.doi.org/10.5772/60886

$$\gamma_{lv}\cos\theta = \gamma_{sv} - \gamma_{sl}, \quad (1)$$

where γ_{sv}, γ_{sl}, and γ_{lv} are the surface energies corresponding to the solid–vapor, solid–liquid, and liquid–vapor interfaces, respectively, and θ is the contact angle. Figure 1 shows various degrees of wetting as quantified by the contact angle. Small contact angles (<< 90°) correspond to high wettability, while large contact angles (>> 90°) correspond to low wettability. For water, if the contact angle is smaller than 90°, the solid surface is considered hydrophilic and if the contact angle is larger than 90°, the solid surface is considered hydrophobic. Usually, bare metallic and ceramic surfaces are highly hydrophilic while many polymers exhibit hydrophobic surfaces. Contact angles can be static and dynamic angles. Static contact angles are measured when the droplet is standing on the surface and its three-phase boundary is not moving. When the three-phase boundary is moving, dynamic contact angles can be measured, and they are referred to as advancing and receding contact angles. Contact angle hysteresis is the difference between the advancing and receding contact angles. Advancing and receding contact angles give the maximum and minimum values the static contact angle can have on the surface. Contact angle measurements are used in fields ranging from coatings to printing and to oil recovery.

At the macroscopic scale, the contact angle can be measured by conventional optical techniques, whereas at the micro- and nanoscale, it is only accessible either by more advanced optical techniques, by indirect measurements, or by direct measurements with scanning probe techniques, as will be shown in the following sections.

Scanning probe techniques are also able to measure interaction forces and energies directly, similar to the surface forces apparatus, which will be reviewed in the following section.

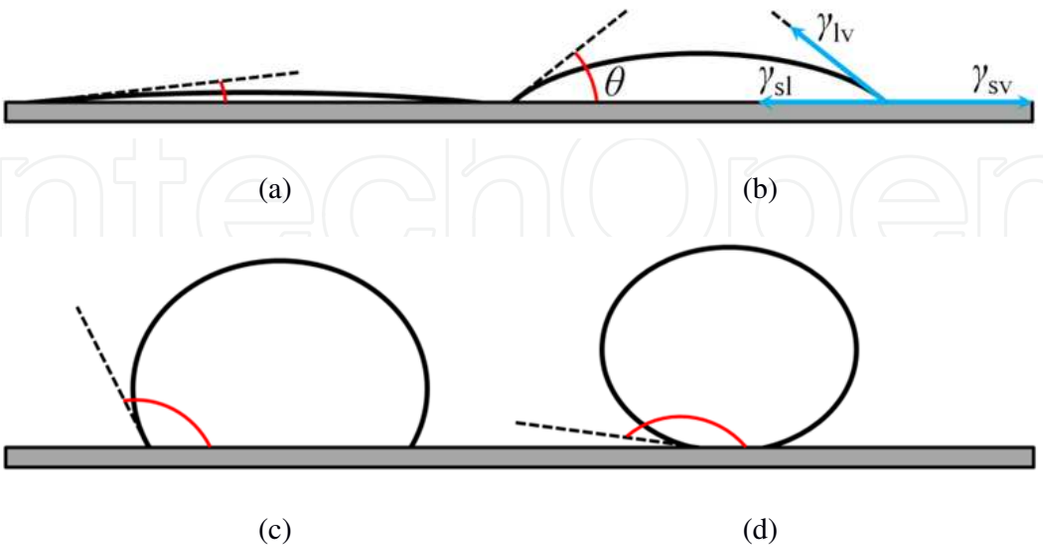

Figure 1. Contact angles for various degrees of wetting: a) almost total wetting, θ ~ 0°; b) good wetting, θ < 90°; c) poor wetting, θ > 90°; d) almost no wetting, θ ~ 180°

2.1. Surface forces apparatus

The surface forces apparatus (SFA), introduced by Tabor, Winterton, and Israelachvili in the 1970s [10-12], enables the determination of the distance dependence of forces between surfaces, with resolution down to 10 nN. The forces are usually measured directly by the deformation of a spring attached to one of the surfaces or by means of capacitive sensors. The surfaces are held close to each other in crossed cylinder geometry (Figure 2). The distance between the surfaces, measured by interferometry with a resolution of ~0.1 nm, is usually controlled by means of piezoelectric positioners. The crossed cylinders usually have the same radius, and this geometry is equivalent – from the point of view of the distance dependence of the forces – to a sphere of the same radius in the vicinity of a plane [13]. The samples are usually deposited (sputtered, adsorbed, etc.) in the form of thin layers on mica sheets, which are bent and fixed to transparent semi-cylindrical lenses. Mica is usually employed because it is transparent and can easily be cleaved to obtain atomically flat surfaces. Initially, the technique was developed for measurements in vacuum or air, and was subsequently extended for liquid and controlled gas environment.

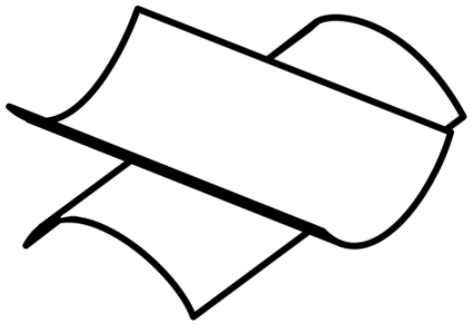

Figure 2. Crossed cylinder geometry of the samples in the surface forces apparatus

One of the samples is attached to a spring cantilever system with known elastic constant and the other sample is attached to the piezoelectric positioning system. The samples are first brought into close vicinity (< 1μm) by a coarse positioning mechanism, usually a stepper motor or a micrometer screw. The distance between the surfaces is measured by an optical technique using fringes of equal chromatic order (FECO), in a white light interferometer. The separation between the surfaces, their shape as well as the refractive index of the material between them, can be calculated from the positions and shapes of the fringes. The piezoelectric positioner moves one of the samples by a controlled amount. The deformation of the spring holding the other sample can be determined from the optically measured distance between the samples, and thus the force can be calculated.

This technique has allowed the accurate determination of fundamental interactions between surfaces: van de Waals, electric double layer, adhesion, capillary, solvation, hydration, steric, hydrophobic, etc. It has also been extended to measuring lateral forces (shear and friction) and forces in the dynamic regime. The SFA technique can now be used to measure both normal and lateral forces between surfaces in liquids with a distance resolution of less than 1Å, and it

http://dx.doi.org/10.5772/60886

can be involved even in measuring forces in electrochemical and biological systems [14]. Additionally, SFA can be combined with complementary techniques, such as AFM [15], X-ray scattering [16], IR spectroscopy, and fluorescence microscopy [17], in order to be able to perform different measurements at the same time on the same sample.

2.2. Wilhelmy method

In the Wilhelmy method, the contact angle is determined indirectly by measuring the force exerted on a solid sample of simple shape (plate, rod, wire, etc.), which is brought in contact with a liquid (Figure 3). The Wilhelmy method finds nowadays wide use in the preparation and monitoring of Langmuir–Blodgett films.

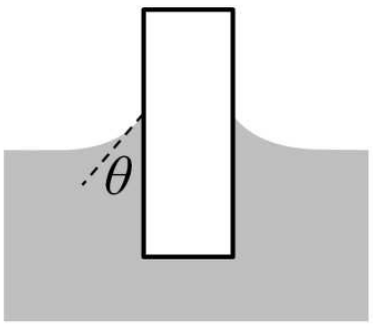

Figure 3. Formation of the liquid meniscus when the sample is submerged in a wetting liquid

The force is usually detected by a sensitive balance which measures the apparent weight of the sample as it is inserted into and retracted out of the liquid (Figure 4a). The apparent weight (G_{app}) at any moment is the sum of the actual weight (G), the wetting force and the buoyancy:

$$G_{app} = G + \gamma_{lv} L cos\theta - \rho V g, \tag{2}$$

where γ_{lv} is the surface tension of the liquid, L is the length of the contact line, θ is the contact angle, ρ is the density of the liquid, V is the submerged volume of the sample, and g is the gravitational acceleration.

The force detected by the balance during a full cycle of insert–retract (submersion cycle) has the general shape described in Figure 4b, and it represents an excellent choice for measuring the dynamic contact angles on any homogeneous, regularly shaped sample. During the initial approach (A), the measured force is actually the weight of the sample. When the sample touches the liquid (B), the surface tension of the liquid creates a relatively sharp increase or decrease of the force – depending whether the liquid wets the sample or not, respectively (Figures 3 and 4 show the case of a wetting liquid). Upon further submersion (C), the increasing buoyancy causes the apparent weight to decrease. In this region the contact angle is the advancing contact angle. While the sample is retracted (D) the contact angle is the receding contact angle. The offset between the C and D portions of the graph is due to the contact angle

hysteresis, which is mainly an effect of the contact line being pinned by defects and irregularities of the sample surface [18-20].

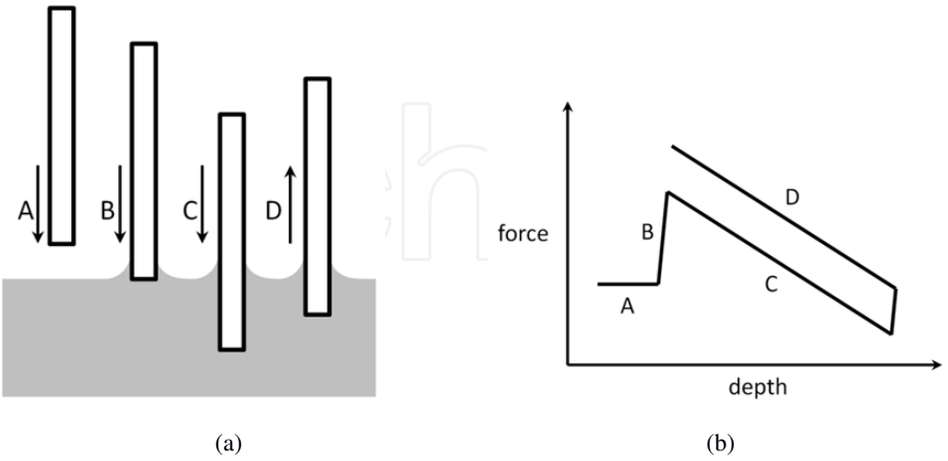

Figure 4. (a) Submersion cycle with the Wilhelmy balance technique; b) the apparent weight of the sample measured by the Wilhelmy balance during a submersion cycle

An adaptation of this technique for measurements at the nanoscale is described in the work of Yazdanpanah [21]. The samples are nanowires with diameters of up to 500 nm, which extend from the apex of AFM tips – so-called nanoneedle probes. The wires, made of Ag_2Ga alloy, are grown at room temperature from droplets of melted gallium, on the surface of silver-coated AFM tips. The forces are conveniently determined with the AFM through force-distance spectroscopy measurements. The buoyancy can be neglected due to the reduced volume of the wires, so the corresponding submersion and retraction portions of the force curves are horizontal (Figure 5). As the diameters of the wires are accessible from SEM measurements, the contact angle values can readily be determined from the force measurements. In the described experiments, for most of the studied liquids, the authors observed only very small contact angle hysteresis, which they attributed to the low dimensions of the defects which would pin the contact line and to the low values of the liquids' surface tensions.

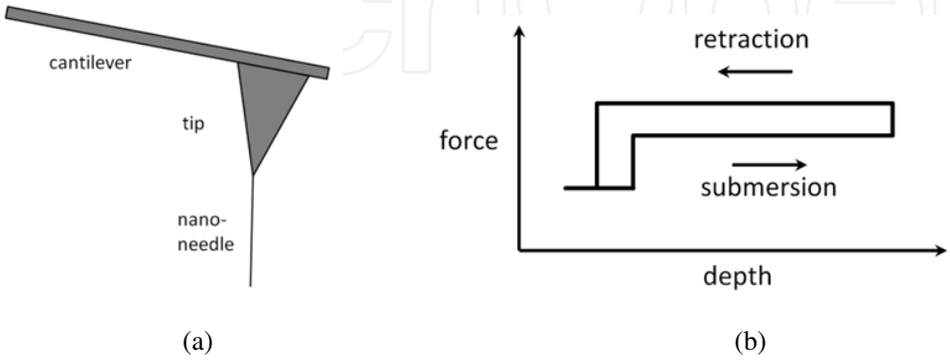

Figure 5. (a) Schematic representation of nanoneedle tips; b) The wetting force measured with the Wilhelmy balance technique at the nanoscale, with nanoneedle tips

http://dx.doi.org/10.5772/60886

2.3. Optical methods

2.3.1. Sessile drop

One of the most widely used techniques for studies of wetting properties is the sessile drop technique, in which the contact angle is directly measured from the profile of a liquid drop. A general setup consists of a horizontal sample stage illuminated from behind, a liquid dispensing syringe or pipette and a visualization system (Figure 6). Early setups used telescopes fitted with a goniometer eyepiece (protractor) to measure visually the contact angle [22]. Modern setups make use of digital video cameras, which allow measurements in the dynamic range and recording data for postprocessing.

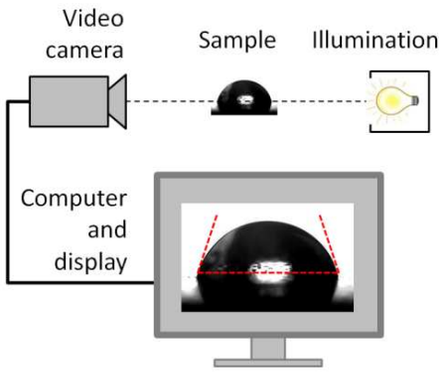

Figure 6. Schematic representation of the contact angle measurement setup for sessile drop technique

If someone intends to characterize solid surface energies, the Sessile Drop method is highly appropriate. Thus, using a liquid having a known surface energy and generating a drop of it on the solid surface to be investigated, from the shape of the drop, the specific contact angle, and the known surface energy of the liquid, one can have enough parameters to calculate the surface energy of the solid sample. In such experiments a specific probing liquid is used, and for a trustable determination of the solid surface energy several different probing liquids should be used.

This method has the advantage of a relatively simple design and operation. It allows a huge variety of samples to be studied: from "standard" materials (polymers, metals, glass, textiles, etc.) [23,24], to films of colloid particles [25-27], layers of bacteria [28,29], or even viruses [30].

2.3.2. Interference microscopy

Interference microscopy allows the determination of the three-dimensional shape of drops on transparent or reflective substrates, and the subsequent calculation of the contact angle. In interference microscopy the contact angle value is calculated using the fringe patterns formed by the interfering beams reflected from the solid–liquid and the liquid–vapor interfaces. In the work described in reference [31], droplet profiles were reconstructed by analyzing the intensity

profiles along the interference pattern (Newton rings) created when observing the droplets from above with an interference microscope. The positions of the intensity maxima and minima were used for the reconstruction of the droplet profiles. This method is only suited for contact angles less than ~30°, and for contact angles lower than 15° it offers high precision.

Fischer and Ovryn describe a method for the reconstruction of droplet profiles for higher values of contact angles, from phase images recorded using sufficiently high numerical aperture objectives in a confocal interference microscope [32]. The method uses a scalar model based on geometrical optics principles, in order to determine the differential optical path length through the droplets. However, this method requires a prior estimation of the shape of the droplets in order to determine the actual exact shape of the droplets, as it needs to be incorporated in an iterative algorithm.

2.4. Scanning probe techniques

2.4.1. Atomic Force Microscopy (AFM)

In atomic force microscopy, a sharp tip is raster-scanned in the vicinity of the sample surface, in the region of the van der Waals forces. A force-sensing mechanism (in most cases a "light lever", as shown in Figure 7), coupled to a feedback loop, which controls the separation between tip and sample, helps maintain a constant interaction force during scanning, allowing the tip to follow the topography of the surface.

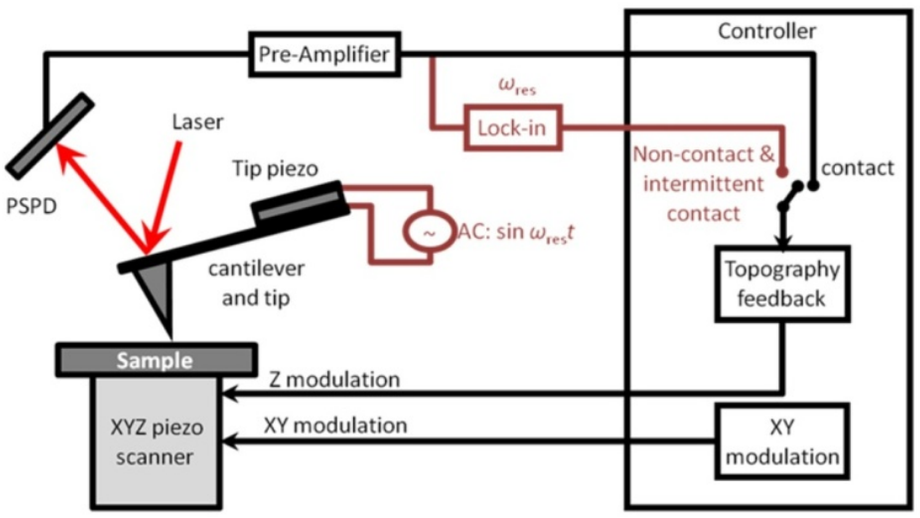

Figure 7. The common light lever technique and the signals in contact and noncontact AFM

Techniques of this family have been employed in studies of wetting phenomena. Yu and coworkers report about the direct measurement of macroscopic contact angles for millimeter size glycerol droplets [33]. The contact angles are determined directly from topography images taken at the edge of the droplets, in noncontact mode. Another study, by Checco and coworkers, reports about noncontact AFM measurements of the topography of micron-sized alkane

droplets [34]. However, the true noncontact regime is difficult to maintain in AFM measurements due to the very low separation between the tip and the liquid surface (< 5 nm), which increases the risk of the tip being captured by the liquid [35,36]. Jung and Bhushan describe a method for the indirect measurement of the contact angle for micro- and nanodroplets of the liquid glycerol mixed with a small amount of rhodamine [37]. A modified AFM tip (NADIS – nanodispenser) is employed for the controlled deposition of micro- and nanodroplets. The contact angle is calculated after measuring the exact volume of the deposited liquid (from the change in resonant frequency of the cantilever before and after releasing the droplet), its height (from force-distance curves taken in the center of the droplet) and diameter (from AFM topography images of the rhodamine trace left on the substrate after evaporation).

2.4.2. Scanning Polarization Force Microscopy (SPFM)

In order to overcome the difficulties of maintaining a noncontact regime in AFM measurements, Scanning Polarization Force Microscopy (SPFM) has been proposed and implemented at the Lawrence Berkeley National Laboratory [38]. The technique is based on the measurement and control of electric polarization forces, which appear when a conductive AFM tip is electrically biased with respect to the sample surface. As the range of electric interaction is larger than the range of van der Waals interaction, the tip can follow the topography contour at a larger distance (typically 10–20 nm) than "classical" noncontact AFM. This makes SPFM a very powerful and versatile technique, which is able to image a large variety of wetting-related processes: from molecularly thin films of water [38], capillary phenomena and adsorption of water on surfaces [39-41], droplets of ionic solutions [36], wetting and corrosion by sulfuric acid [42,43], liquid crystals [44], lubricants [45,46], to bio-membranes and lyposomes [47,48].

The following section describes in detail the SPFM principle and method.

3. SPFM principle and method

3.1. Polarization phenomena and forces

In scanning polarization force microscopy an electrical bias is applied to a conductive AFM tip, which leads to an accumulation of electric charge on the tip. As the physical dimensions of the tip apex are very small (radius on the order of few tens of nanometers), the electric field in its vicinity is greatly enhanced. When the tip is brought in the vicinity of the sample, the strong electric field causes a local accumulation of electric charge of opposed sign, which can be conveniently modeled by the image charge, as shown in Figure 8. The two opposed charges create an attractive electrostatic polarization force with magnitude in the nanonewton range for tip-sample distances of few tens of nanometers and tip bias of a few volts [49]. This force can be detected by the usual AFM light lever technique and is kept constant by the topography feedback loop while scanning the sample, in order to obtain a constant force image.

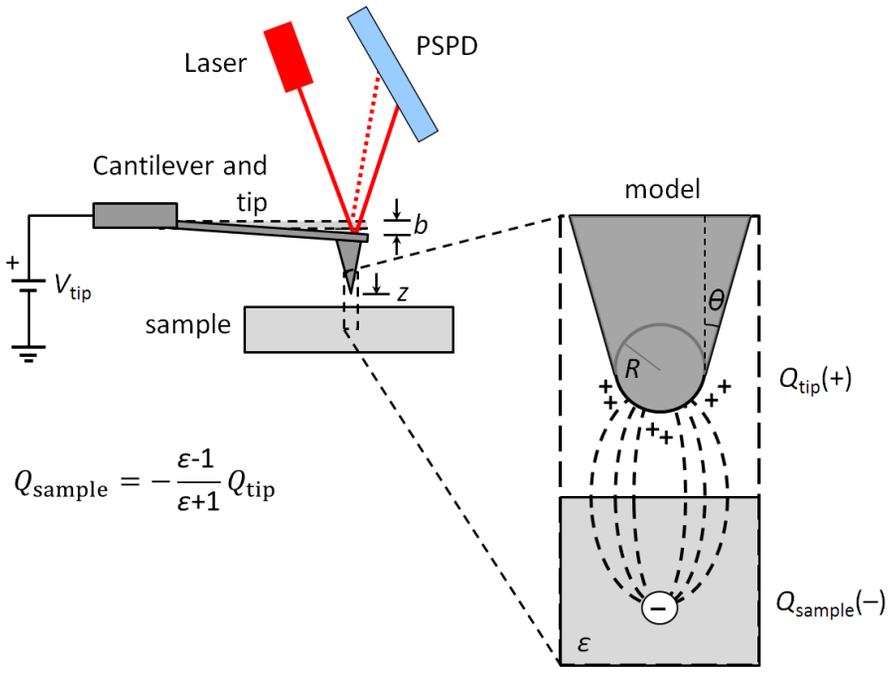

Figure 8. Tip charge and induced image charge with a positive bias applied to the AFM tip

The electrostatic force acting on the tip can be written as [49,50]:

$$F = -\frac{1}{2}\frac{\partial C}{\partial z}\left(V_{\text{tip}} - V_{\text{CPD}}\right)^2 \cong -4\pi\varepsilon_0 \frac{\varepsilon - 1}{\varepsilon + 1} f\left(\frac{R}{z}\right)\left(V_{\text{tip}} - V_{\text{CPD}}\right)^2, \tag{3}$$

where C is the tip-sample capacitance and V_{CPD} is the local contact potential difference. The function $f(R/z)$ is characteristic of the tip-sample geometry. Although it is basically impossible to calculate an exact analytical expression of this function, some approximations can provide useful results.

If the tip and cantilever are approximated by a sphere plus a flat plate, the resulting contributions to the capacitance are

$$C_{\text{tip}}(z) \cong 2\pi\varepsilon_0 R(\ln\frac{R}{z} + 2) \text{ and } C_{\text{lever}}(z) \cong \frac{\varepsilon_0 S}{z + D}, \tag{4}$$

where S is the area of the plate corresponding to the tip and D is the separation between the model sphere and the plate [49]. For typical values of these parameters found in practice (e.g., R = 100 nm, z = 10 nm, S = 1000 μm², D = 5 μm), it is found that the lever capacitance exceeds the tip capacitance by two orders of magnitude. However, the corresponding forces, $\partial C_{\text{tip}}/\partial z$ and $\partial C_{\text{lever}}/\partial z$, are comparable. Moreover, because $z \ll D$, $\partial C_{\text{lever}}/\partial z$ is almost insensitive to variations of z, while $\partial C_{\text{tip}}/\partial z$ follows the topography.

From equation (4), in the range $z < R$, the electrostatic force can be approximated by the following function [49]:

$$F \cong \left(\frac{AR}{z} + B\right)\left(V_{\text{tip}} - V_{\text{CPD}}\right)^2, \tag{5}$$

where A and B are constants on the order of 10^{-11} N/V^2 each. It can be seen that in this region the force has a 1/z dependence.

4. Comparison of SPFM with AFM

As the separation between tip and sample is larger in SPFM than in standard contact and noncontact AFM operations, the risk of the tip touching the surface is minimized. This is especially useful in studies of soft and liquid samples, where contact AFM cannot be considered at all for topography measurements and noncontact AFM is generally difficult to operate.

However, this leads to a loss of lateral resolution compared to standard AFM. In SPM, generally, the lateral resolution cannot be less than the tip-sample separation, and is also influenced by the dimensions of the tip apex. So in most of the SPFM experiments the lateral resolution is on the order of few tens of nanometers. The vertical resolution does not suffer from this loss and is limited by the noise level of the system, usually better than one nanometer.

4.1. DC-SPFM

In DC-SPFM the bias applied to the tip is constant, and the electric polarization force has the form described by equation (3). It can be seen that besides topographical influence (accounted for by the function f), the force is dependent on variations of the local dielectric constant of the sample. For constant force topography imaging this will reflect in an apparent topography contrast for adjacent areas of the sample having the same height and different dielectric constants. This is perfectly illustrated in the studies of Hu and coworkers [36,38] where the first layers of water adsorbed on the hydrophilic surface of freshly cleaved mica were imaged in DC-SPFM in increasing relative humidity. It was found that two distinct phases exist, and the topography contrast indicated a difference in dielectric constant between the two. Moreover, the shape of one of the phases' domains suggests a crystalline structure for this phase.

4.2. AC-SPFM

In AC-SPFM, the bias applied to the tip has an AC and a DC component: $V_{\text{tip}} \sin \omega t + V_{\text{DC}}$. Equation (3) will give

$$F \cong -4\pi\varepsilon_0 \frac{\varepsilon - 1}{\varepsilon + 1} f\left(\frac{R}{z}\right)\left(V_{\text{tip}}\mathbf{sin}\omega t + V_{\text{DC}} - V_{\text{CPD}}\right)^2 =$$

$$= -4\pi\varepsilon_0 \frac{\varepsilon - 1}{\varepsilon + 1} f\left(\frac{R}{z}\right)\left[-\frac{1}{2}V_{\text{tip}}^2\mathbf{cos}2\omega t + 2V_{\text{tip}}\left(V_{\text{DC}} - V_{\text{CPD}}\right)\mathbf{sin}\omega t + \frac{1}{2}V_{\text{tip}}^2 + \left(V_{\text{DC}} - V_{\text{CPD}}\right)^2\right] = \tag{6}$$
$$= F\left(2\omega\right) + F\left(1\omega\right) + F\left(0\omega\right)$$

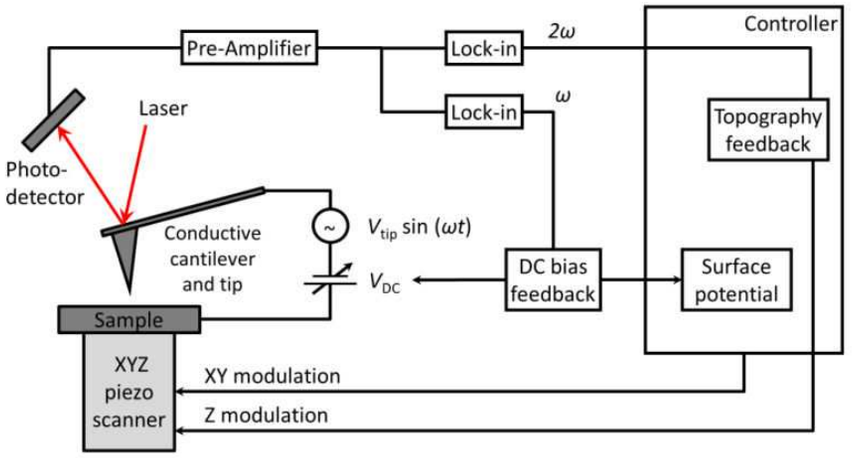

Figure 9. Schematic view of the SPFM setup

The polarization force has three components with different time dependencies: 2ω, 1ω, and a DC component. The 2ω and 1ω components can be separated with the use of lock-in amplifiers. The amplitude of the 2ω component is used for constant force topography feedback. The amplitude of the 1ω component can be used to determine V_{CPD}: a feedback loop which controls the value of V_{DC} is set to null the amplitude of the 1ω component, which, as seen in equation (6), happens when V_{DC} equals V_{CPD}. Figure 9 shows a common setup for SPFM experiments.

4.3. Forces and energies in wetting at nanoscale

For macroscopic drops, where most of the liquid is outside the range of long-range forces, the contact angle is defined as the angle at which the liquid surface meets the substrate, measured through the liquid (Figure 10a). For micron and nanometer size droplets, where most of the liquid is affected by the long range forces, the liquid meniscus does not meet the substrate at a well-defined angle (Figure 10b). The effective contact angle, further called microscopic contact angle, is determined by the slope of the droplet profile at the inflexion points [43].

Figure 10. Contact angle for a) macroscopic droplets; b) microscopic and nanometer size droplets

In order to study the wetting behavior of nanodroplets, following a similar approach of de Gennes [49,51,52], the effect of long-range forces will be analyzed. The free energy for a circularly symmetric drop defined by the shape $z(r)$ can be written as an integral over the area covered by the drop:

http://dx.doi.org/10.5772/60886

$$G = G_0 + \int_{\text{drop}} 2\pi r \, \mathbf{d}r \left[-S + \frac{\gamma_{\text{lv}}}{2} \left(\frac{\mathbf{d}z}{\mathbf{d}r} \right)^2 + P(z) - \frac{\mu_{\text{vapor}} - \mu_{\text{liq}}}{v_{\text{mol}}} \cdot z \right] \tag{7}$$

The first term under the integral that characterizes the wetting properties of a surface by a given liquid is the spreading coefficient, $S = \gamma_{\text{sv}} - \gamma_{\text{sl}} - \gamma_{\text{lv}}$, where γ_{sv}, γ_{sl}, and γ_{lv} are the surface energies corresponding to the solid–vapor, solid–liquid and liquid–vapor interfaces, respectively. Valid for the case of shallow droplets is the second term, which is due to the excess surface caused by the curvature of the drop. The third term $P(z)$ is the surface potential energy between the surfaces. The supersaturation in terms of chemical potentials of the vapor and liquid is described by the last term; v_{mol} is the molecular volume of the liquid [51].

Considering a constant volume of droplet, $V = \int z(r) \; 2\pi r \; \mathrm{d}r$, and assuming that the droplets have spherical cap shape [52], the minimization of the free energy G in equation (7) leads to the relation between the microscopic contact angle θ, the surface potential $P(e)$, and the disjoining pressure defined as $\Pi(e) = -\frac{\mathrm{d}P}{\mathrm{d}e} = -P'(e)$ [53]:

$$\theta^2 = \theta_0^2 + \frac{2}{\gamma} \left[P(e) + e\Pi(e) \right], \tag{8}$$

where e is the height of the droplet, θ_0 is the macroscopic contact angle, $P(0)$ is the spreading coefficient S which characterizes the wetting properties of a surface by a given liquid at short ranges. If $S > 0$ the liquid will completely wet the surface; if $S < 0$ a contact angle will exist, determined by Young's equation $\gamma_{\text{lv}} \cos\theta = \gamma_{\text{sv}} - \gamma_{\text{sl}}$. Thus, the contact angle θ is influenced by the disjoining pressure and depends on the interfacial energies. The disjoining pressure is related to the spreading coefficient S by

$$S = \int_0^\infty \Pi(x) dx = P(e)_{e \to 0} \tag{9}$$

By rearranging the terms of equation (8) it can be obtained that

$$P(e) - eP'(e) = \left(\theta^2 - \theta_0^2 \right) \frac{\gamma}{2} \tag{10}$$

Thus, using the dependence described in equation (10), the potential energy $P(e)$ between the surfaces can be quantitatively determined after measuring the dependence of contact angle on droplet height in the case of spherical shaped droplets of small height. The ability of SPFM to image the topography of liquid samples makes it an ideal candidate for such determinations, as described in the following section.

5. Application of SPFM techniques for nanometer scale wetting investigations

This section presents results regarding the characterization of wetting properties at nanoscale, obtained in the Center for Surface Science and NanoTechnology (CSSNT) at the University "Politehnica" of Bucharest. The results were reported in references [54-56].

5.1. Wetting properties of glycerol and sulfuric acid on highly oriented pyrolitic graphite and aluminum

In this study, glycerol and sulfuric acid were chosen for the formation of liquid droplets on highly oriented pyrolytic graphite (HOPG); on aluminum-covered mica, the droplets were formed by glycerol [54].The HOPG substrates were freshly cleaved prior to the experiments. The aluminum film was deposited on freshly cleaved mica by thermal evaporation in vacuum. The substrates were verified by optical microscopy prior to the deposition of liquid droplets. In order to create the droplets, an evaporation–condensation technique was chosen: a few milliliters of glycerol were heated in a Berzelius glass to ~100°C. The substrates were held upside down at ~5 mm above the liquid until their surface achieved a "foggy" appearance, which indicated the presence of microscopic droplets. Optical microscopy (Figure 11a and c) confirmed the presence of small droplets [54].

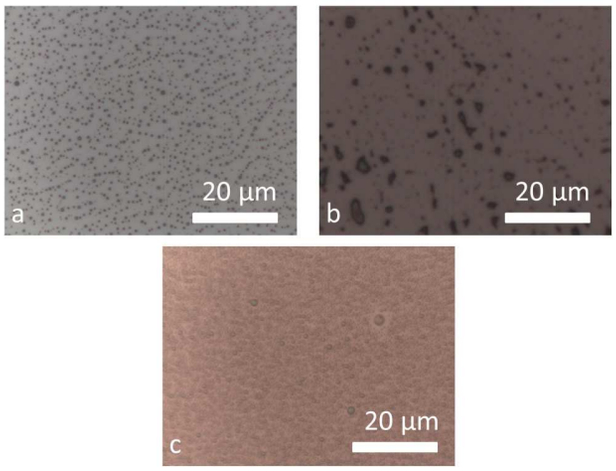

Figure 11. Optical microscopy images of the samples after the deposition of the droplets: a) glycerol on HOPG; b) sulfuric acid on HOPG; c) glycerol on aluminum-covered mica

Sulfuric acid droplets (50% vol.) were created on the substrates by casting a macroscopic drop (~50 µl) and then absorbing the liquid at one corner of the substrate with the aid of a lens-cleaning tissue, avoiding contact between the tissue and the substrate surface. The substrates appeared dry at a first inspection with the naked eye. However, optical microscopy images revealed the presence of liquid droplets of various sizes and shapes (Figure 11b) [54]. The droplet deposition took place at room temperature and ~50% relative humidity. The images shown in Figure 11 are typical for the distribution of glycerol and H_2SO_4 droplets on the substrates.

Figure 12 shows typical SPFM-AC topography images of the samples after the deposition of the droplets on HOPG and aluminum. The images show that the dispersion of the droplets depends on liquid type and substrate. The deposited droplets have shapes close to spherical caps, which allows us to use the theoretical model of de Gennes [51] in order to determine the surface potential energy $P(e)$ between glycerol/H_2SO_4 and HOPG and between glycerol and aluminum.

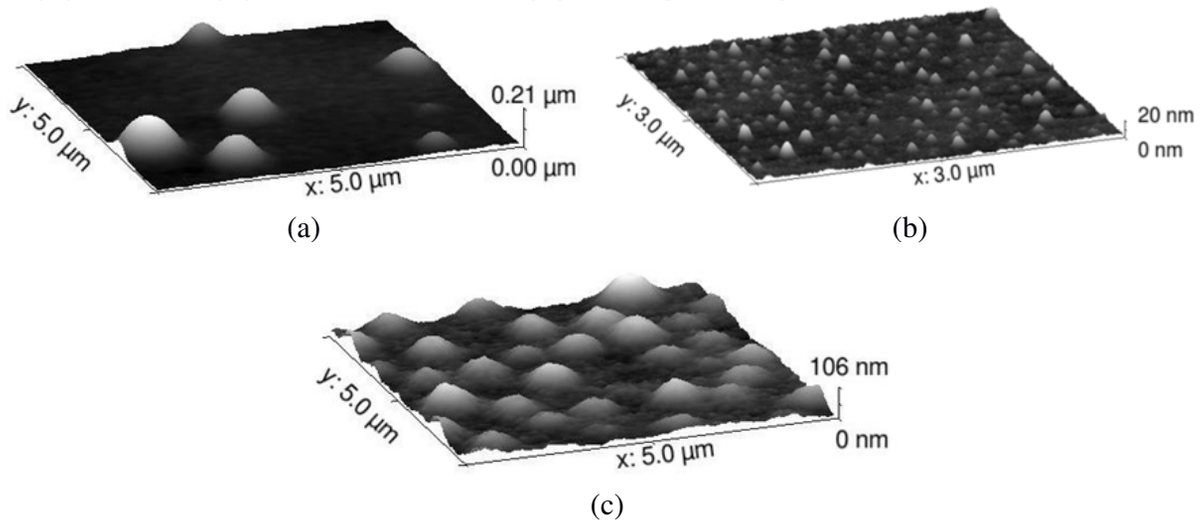

Figure 12. Typical SPFM-AC images of the samples after the deposition of the droplets: a) glycerol on HOPG, 5 µm × 5 µm; b) sulfuric acid on HOPG, 3 µm × 3 µm; c) glycerol on aluminum-covered mica, 5 µm × 5 µm

Topography profiles of some of the droplets are shown in Figure 13, for glycerol and sulfuric acid on HOPG, and for glycerol on aluminum. The profiles are plotted along segments that pass through the point of maximum height for each chosen droplet [54].

For micro- and nanodroplets, as can be seen in Figure 13 and as discussed in Section 3.e, the liquid meniscus does not meet the solid surface at a precise angle and the graph of the line-cut profile has two inflection points (one on each side of the peak). The contact angle is calculated by measuring the slope (first derivative) of the line-cut profile at these inflection points [35]. Contact angle values corresponding to the droplets were plotted as a function of droplet height. Figures 14 and 15 show the results for glycerol and H_2SO_4 on HOPG and aluminum-covered mica [54]. A decrease of contact angle with droplet height is observed for all cases, which indicates that the surface potential $P(e)$ is negative, i.e., the interaction forces between surfaces are hydrophobic or attractive.

Using relation $\theta^2 = \theta_0^2 + \frac{2}{\gamma}[P(e) + e\Pi(e)]$ and the dependence of contact angle on droplet height (Figures 14 and 15), we calculated the dependence of surface potential energy $P(e)$ between the surfaces for glycerol/H_2SO_4 on HOPG and for glycerol on aluminum-covered mica. The results are shown in Figures 16 and 17. The macroscopic contact angle θ_0 was determined as an asymptotic fitting parameter for the microscopic contact angle dependencies. In a related experiment we measured the macroscopic contact angle by optical methods and the results are in good agreement with the value found in literature [33].

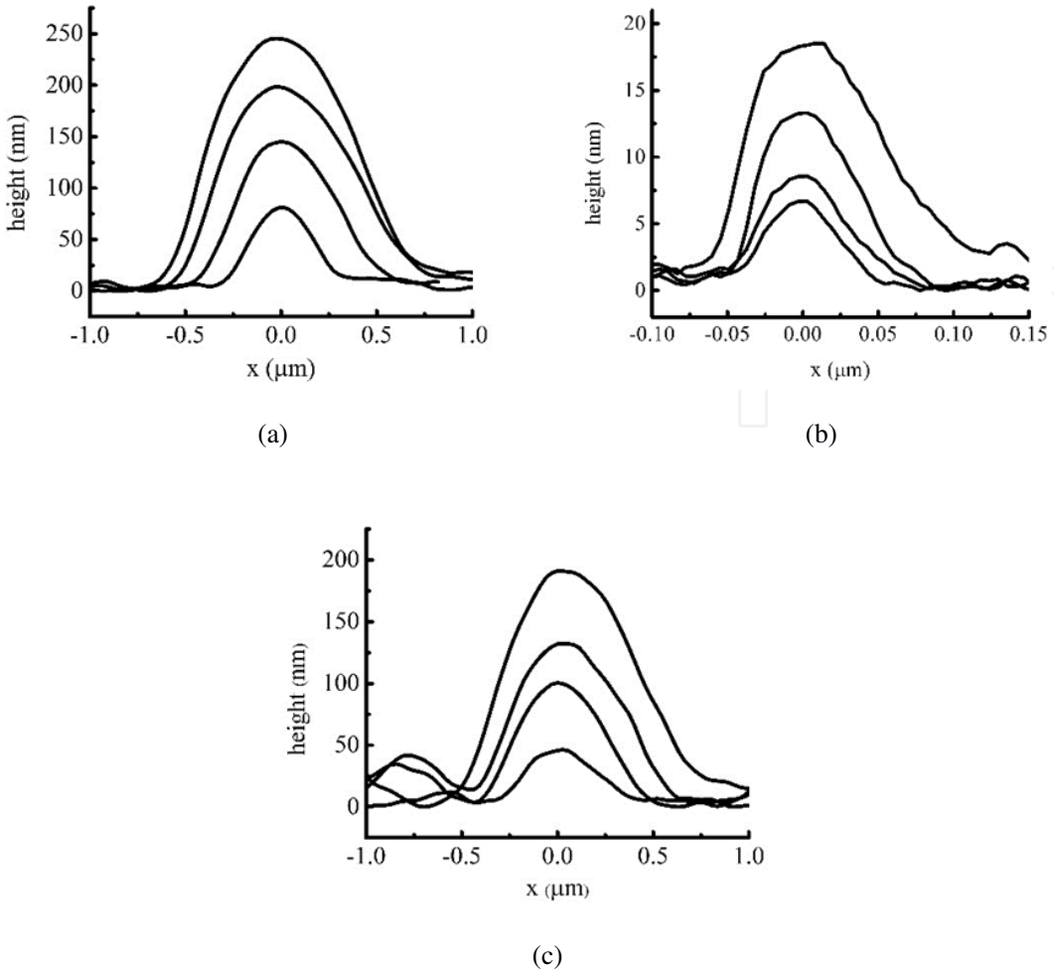

Figure 13. Line-cut profiles of droplets of: a) glycerol on HOPG; b) sulfuric acid on HOPG; c) glycerol on aluminum

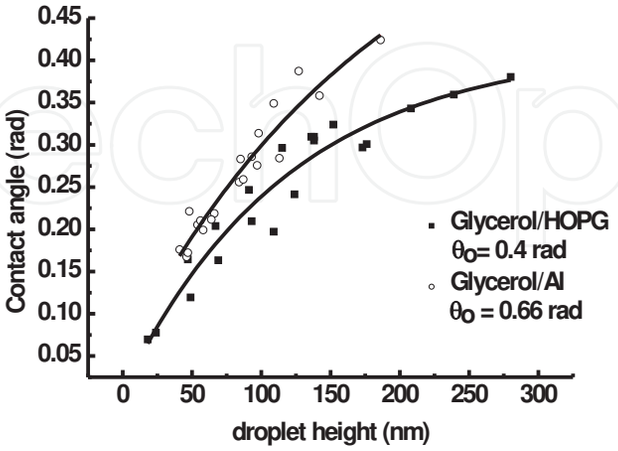

Figure 14. Dependence of contact angle on droplet height for glycerol deposited on HOPG and on aluminum-covered mica

http://dx.doi.org/10.5772/60886

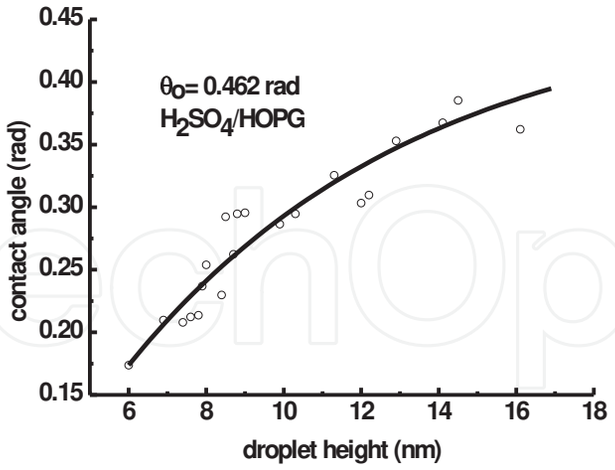

Figure 15. Dependence of contact angle on droplet height for H_2SO_4 deposited on HOPG

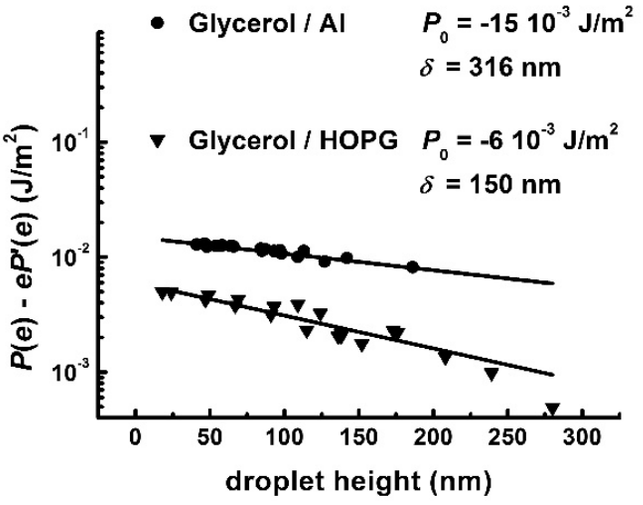

Figure 16. Semilog plot of $P(e) - eP'(e)$ vs. e for glycerol deposited on HOPG and on aluminum-covered mica

On HOPG and aluminum, glycerol and H_2SO_4 form droplets whose shapes are close to spherical caps. The contact angle varies with height as shown in Figures 14 and 15. The decrease of the contact angle with decreasing droplet height indicates that the surface potential $P(e)$ is negative and an exponential dependence $P(e)=P_0\exp(-e/\delta)$ [52] with distance gives a good fit (Figures 16 and 17). From the fitting parameters, P_0 and δ, we determine the dependence of the potential energy on droplet height [54]:

$$P\left(e\right) = -6\cdot 10^{-3}\exp\left(-e/150\ \mathbf{nm}\right)\mathbf{J/m^2}\ \textbf{for glycerol on HOPG}$$

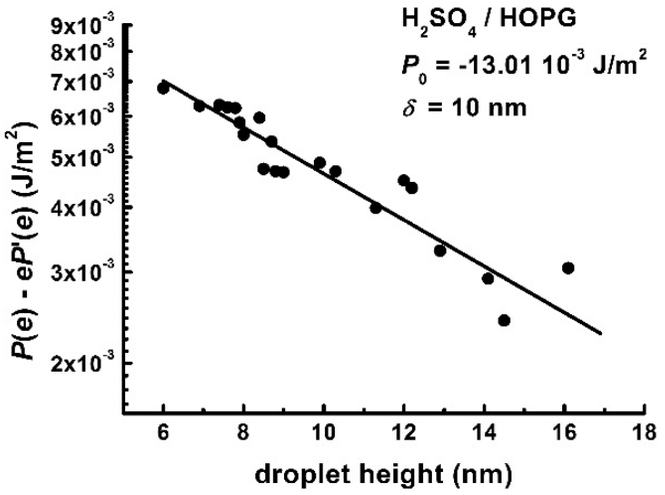

Figure 17. Semilog plot of $P(e) - eP'(e)$ vs. e for H_2SO_4 on HOPG

$$P(e) = -15 \cdot 10^{-3} \exp(-\mathbf{e} / 316\ \mathbf{nm})\ \mathbf{J/m^2}\ \textbf{for glycerol on Al}$$

$$P(e) = -13 \cdot 10^{-3} \exp(-e / 10\ \mathbf{nm})\ \mathbf{J/m^2}\ \textbf{for } \mathbf{H_2SO_4}\ \textbf{on HOPG}$$

The exponential dependence of surface potential energy $P(e)$ in all cases indicates attractive interaction between the liquid–substrate interfaces, having a decay length δ = 150 nm for glycerol on HOPG, δ = 316 nm for glycerol on aluminum, and δ = 10 nm for H_2SO_4 on HOPG, which dominate over the characteristic length of the van der Waals interactions. In our calculations we have used the values of 73 mJ/m^2 and 64 mJ/m^2 for the surface tensions of H_2SO_4 solution and glycerol, respectively.

The strength of the potential at e = 0 nm gives the spreading coefficient S for each liquid on the respective substrate [54]:

$$S = P(0) = -6 \cdot 10^{-3}\ \mathbf{J/m^2}\ \textbf{for glycerol on HOPG}$$

$$S = P(0) = -15 \cdot 10^{-3}\ \mathbf{J/m^2}\ \textbf{for glycerol on Al}$$

$$S = P(0) = -13 \cdot 10^{-3}\ \mathbf{J/m^2}\ \textbf{for } \mathbf{H_2SO_4}\ \textbf{on HOPG}$$

In the case of glycerol on HOPG and on aluminum, the values for spreading coefficient indicate a very weak hydrophobic interaction by comparison with surface tension of glycerol; the value for spreading coefficient indicates a value ten times (on HOPG), respectively, four times (on Al) smaller compared to the surface tension of glycerol, and in the case of H_2SO_4 on HOPG the

value for spreading coefficient indicates a value five times smaller compared to the surface tension of H_2SO_4. These potential energies give negative disjoining pressures Π of ~0.4 atm at e close to zero for glycerol on HOPG, 0.47 atm for glycerol on aluminum and ~13 atm for H_2SO_4 on HOPG. In the case of H_2SO_4 on HOPG the strength of the force appears to be thirty times bigger than that for glycerol on HOPG or aluminum.

5.2. Wetting properties of glycerol on mica and stainless steel

Glycerol was chosen for the formation of liquid droplets in these experiments and the substrates were mica and stainless steel [55].

Mica substrates were freshly cleaved prior to the experiments. Stainless steel substrates were polished using various grades of abrasive paper (gradually increasing the grit) and finally using slurry of alumina particles approximately 20 nm in size, dispersed on a felt disc. They were then sonicated for several cycles in methanol and deionized water for five minutes per cycle.

Glycerol droplets were created on the substrates by condensation, as described in section 4.a. The presence of microscopic droplets was confirmed by optical microscopy inspection (Figure 18).

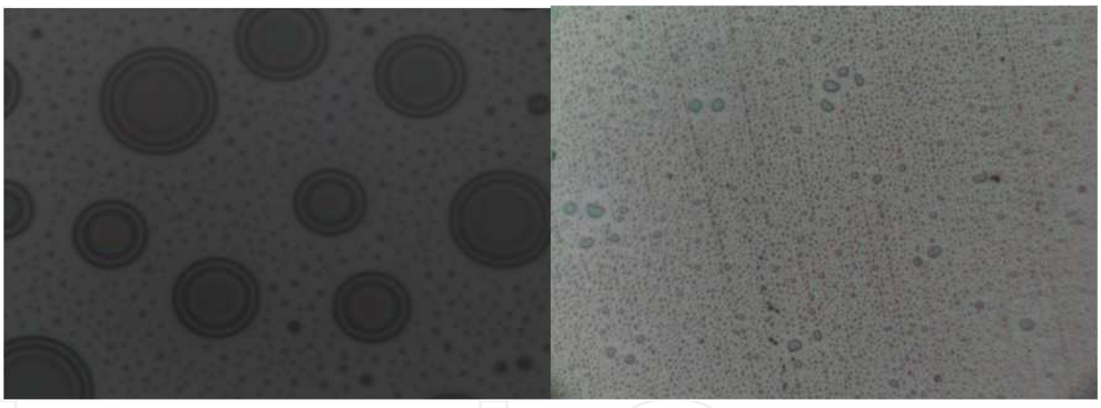

Figure 18. Optical microscopy images of the substrates after the deposition of the droplets: a) glycerol on mica; b) glycerol on stainless steel. Field of view ~80 μm × 64 μm

Optical images shown in Figure 18 are typical for the distribution of glycerol droplets on the substrates in these experiments. On mica, glycerol tends to form many small droplets and few large droplets, while on stainless steel it only forms many small droplets. This could be attributed to the higher roughness of the steel surface, which prevents the droplets form migrating on the surface and merging into larger droplets [55].

Figure 19 shows typical SPFM-AC topography images of the samples after the deposition of the droplets. These images confirm the general aspect of the droplets from the optical microscopy analysis.

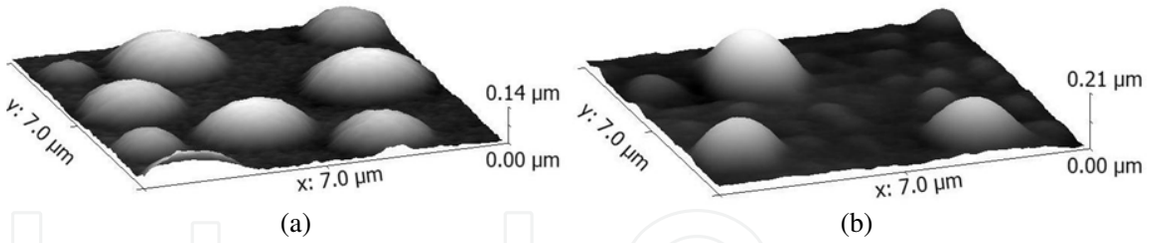

(a) (b)

Figure 19. Typical SPFM-AC images of the deposited droplets of glycerol on: a) mica, b) stainless steel; field of view 7 µm × 7 µm

Droplet profiles were extracted from the SPFM topography images of the samples. Some of the profiles are plotted in Figure 20 [55].

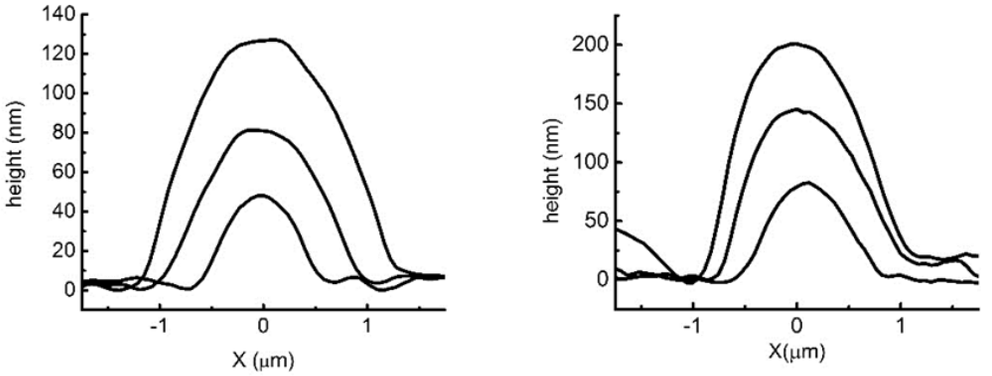

(a) (b)

Figure 20. Line-cut profiles of droplets of glycerol on: a) mica b) stainless steel

Contact angle values corresponding to the droplets were plotted as a function of droplet height (Figure 21) [55]. A decrease of contact angle with droplet height is observed, which indicates that the surface potential $P(e)$ is negative, i.e., the interaction forces between surfaces are attractive or hydrophobic.

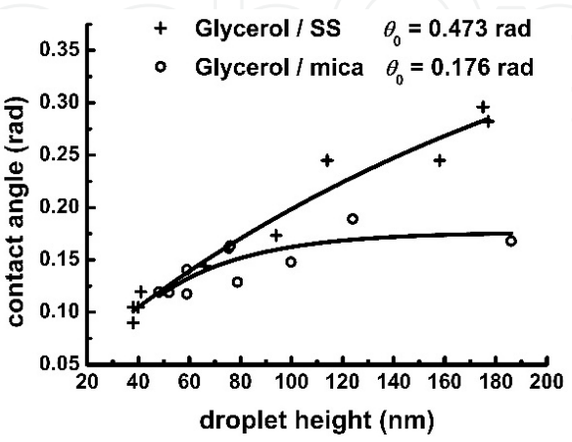

Figure 21. Dependence of contact angle on droplet height for glycerol on mica and stainless steel

http://dx.doi.org/10.5772/60886

Using relation (10) and the dependence of contact angle on droplet height (Figure 21), the height dependence of the term $P(e)–eP'(e)$ for glycerol on mica and stainless steel was determined. The results are shown in Figure 22.

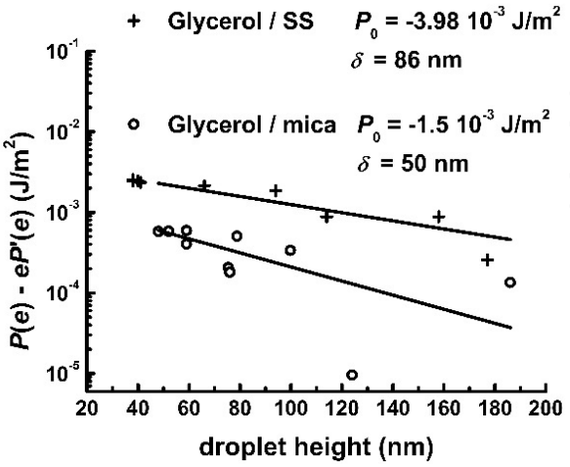

Figure 22. Semilog plot of $P(e)–eP'(e)$ vs. e for glycerol on stainless steel and mica

The decrease of contact angle with decreasing droplet height indicates that the surface potential $P(e)$ is negative and an exponential dependence $P(e)=P_0\exp(-e/\delta)$ [52] with distance gives a good fit (Figure 22), where P_0 and δ are the fitting parameters. From the fitting parameters we determine the dependence of the potential energy on droplet height [55]:

$$P(e) = -1.4 \cdot 10^{-3} \exp(-e / 50\ \mathbf{nm})\ \mathbf{J/m^2}\ \textbf{for glycerol on mica}$$

$$P(e) = -3.98 \cdot 10^{-3} \exp(-e / 86\ \mathbf{nm})\ \mathbf{J/m^2}\ \textbf{for glycerol on stainless steel}$$

The exponential dependence of surface potential energy $P(e)$ with distance indicates hydrophobic attractive forces between the glycerol–mica/stainless steel interfaces, having a decay length $\delta = 50$ nm for glycerol on mica and $\delta = 86$ nm for glycerol on stainless steel, values which dominate over the range of van der Waals forces. These forces may include double layer, solvation, and hydration forces.

The strength of the potential at $e = 0$ nm gives the spreading coefficient [55]:

$$S = P(0) = -1.4 \cdot 10^{-3}\ \mathbf{J/m^2}\ \textbf{for glycerol on mica}$$

$$S = P(0) = -3.98 \cdot 10^{-3}\ \mathbf{J/m^2}\ \textbf{for glycerol on stainless steel}.$$

In both cases, the values for spreading coefficient indicate a very weak hydrophobic interaction for these systems, compared to the surface tension of glycerol. These potential energies give a negative disjoining pressure Π of 0.28 atm for glycerol on mica and 0.46 atm for glycerol on stainless steel. As we see, in the case of the glycerol on stainless steel the strength of the disjoining pressure appears to be two times higher than that for glycerol on mica system.

5.3. Wetting properties of glycerol on silicon, native SiO_2, and bulk SiO_2

Glycerol was chosen for the formation of liquid droplets on silicon, native SiO_2, and bulk SiO_2 [56]. The substrates were prepared as follows: silicon (*p*-type Si(100)) and bulk SiO_2 were washed in ultrapure water and acetone, in an ultrasonic bath, for the removal of organic contamination. Silicon substrates were treated for one minute in HF solution (20% wt.), in order to remove the native oxide layer and to expose the bare silicon surface. The substrates were free of macroscopic defects and impurities over relatively large areas (several mm^2), as revealed by optical microscopy examination (images not shown).

Glycerol droplets were created on the substrates by condensation, as described in Section 4.a. Figure 23 shows optical microscopy images of the substrates after the same deposition time. As can be seen, the droplets are smaller and denser on silicon. We attributed this to the nanoscale roughness of the bare silicon surface resulting after the wet etching. The droplets might become pinned to the surface defects, which would prevent the small droplets coalescing into bigger ones [56].

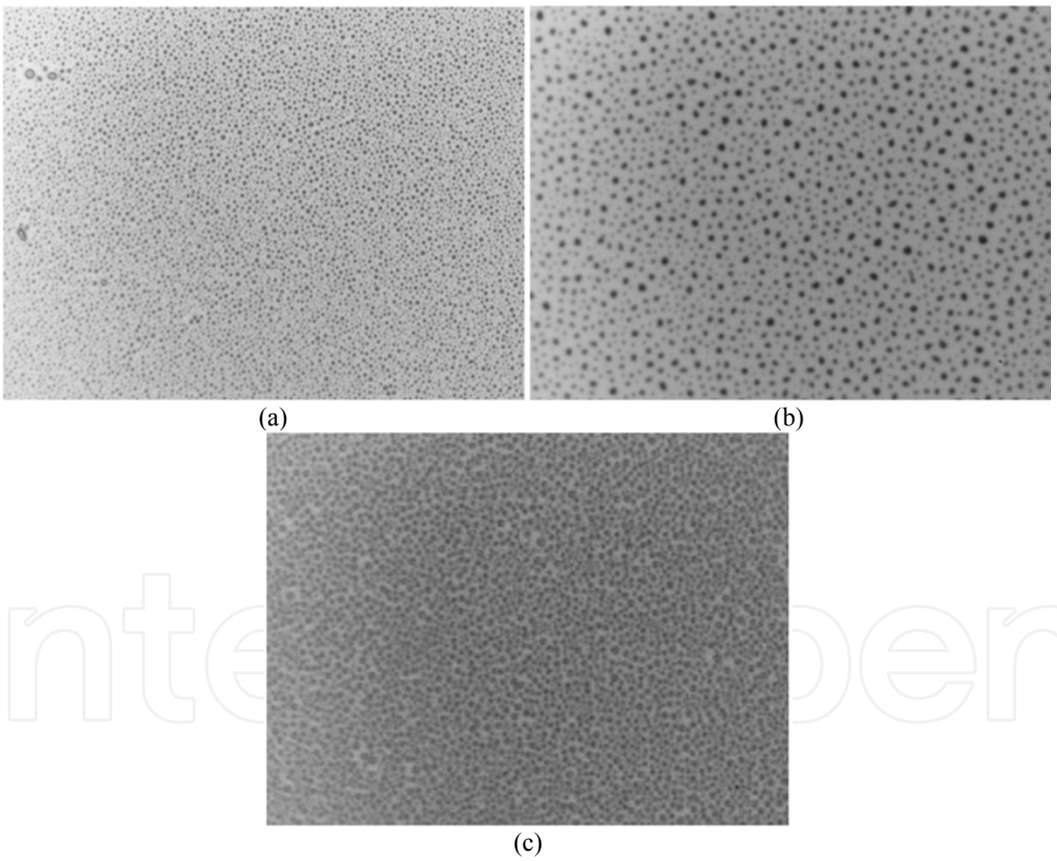

Figure 23. Optical microscopy images of the samples after the deposition of the nanodroplets: a) glycerol on Si; b) glycerol on native SiO_2; c) glycerol on bulk SiO_2. Field of view ~70μm × 55μm

Figure 24 shows typical SPFM-AC topography images of the samples after the deposition of the droplets on silicon, native SiO_2, and bulk SiO_2. The images show that the dispersion of the droplets is strongly influenced by the type of substrate.

http://dx.doi.org/10.5772/60886

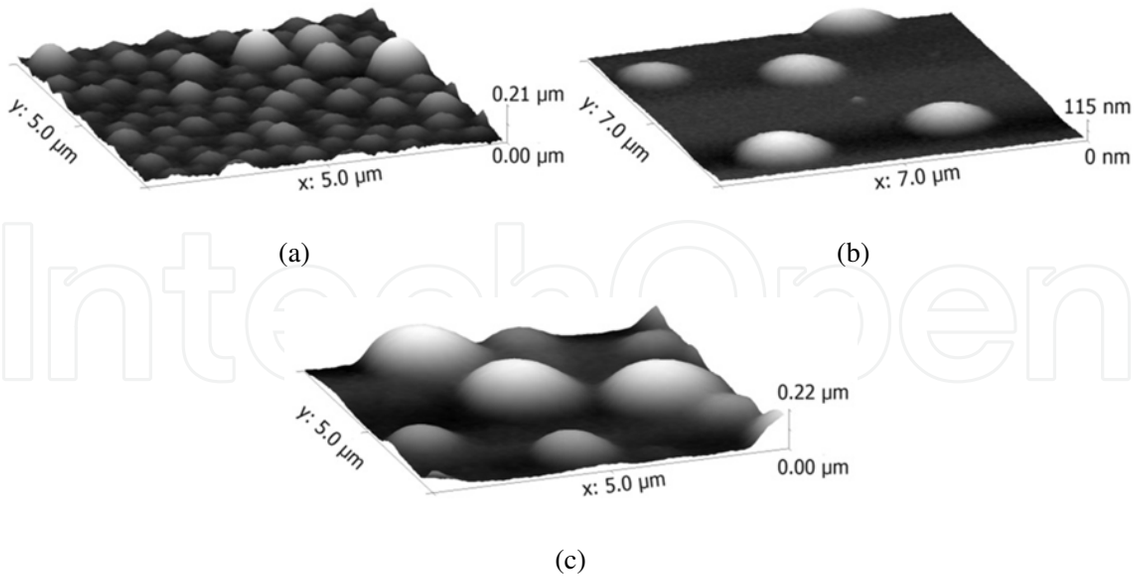

Figure 24. Typical SPFM-AC images of the samples after the deposition of the droplets: a) glycerol on Si, 5µm × 5µm; b) glycerol on native SiO_2, 7µm × 7µm; c) glycerol on bulk SiO_2, 5µm × 5µm

Some of the droplet profiles extracted from the SPFM topography images are plotted in Figure 25 [56].

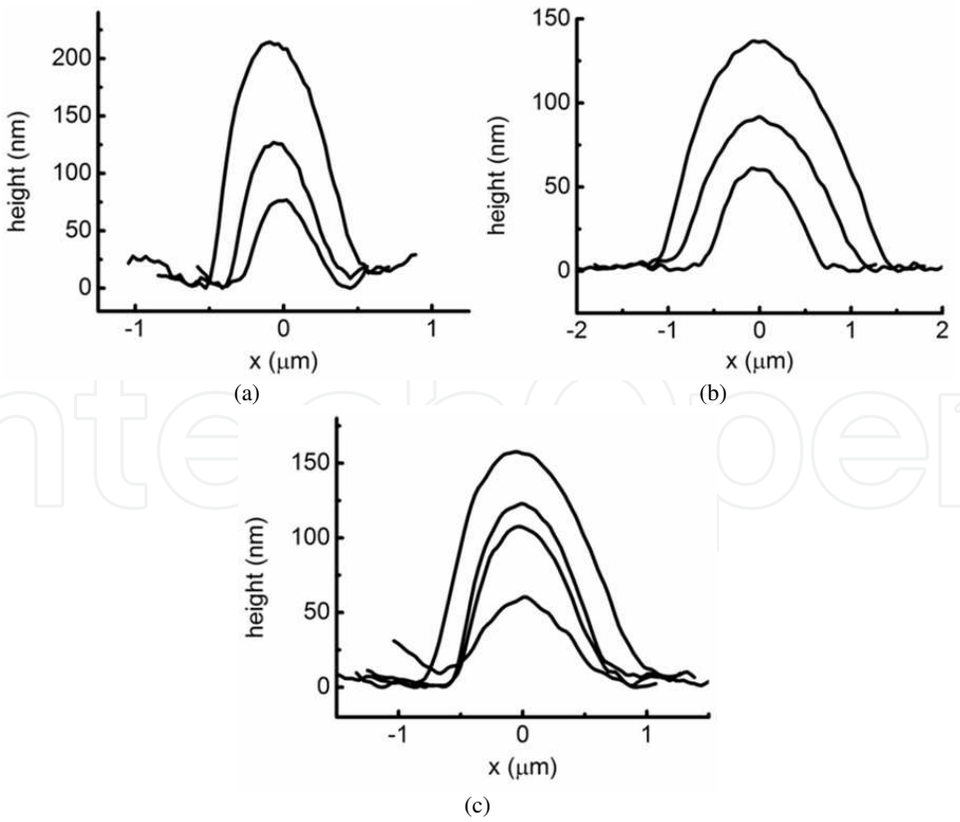

Figure 25. Line-cut profiles of droplets of glycerol on: a) silicon; b) native SiO_2; c) bulk SiO_2

Contact angle values corresponding to droplets such as those shown in Figure 24 (having a circularly symmetric shape) were plotted as a function of droplet height (Figure 26) [56].

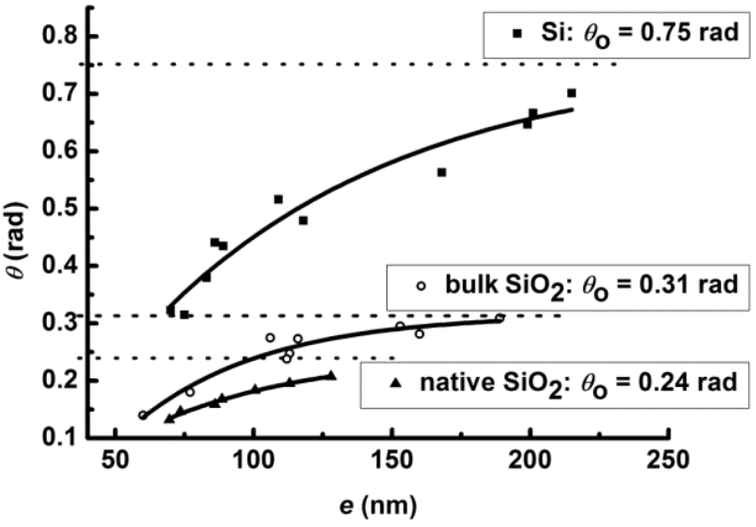

Figure 26. Dependence of contact angle on droplet height for glycerol on silicon, native SiO_2, and bulk SiO_2

The dependence of surface potential energy $P(e)$ on droplet height is calculated from relation $\theta^2 = \theta_0^2 + \frac{2}{\gamma}[P(e) + e\Pi(e)]$, taking into account the measured dependence of contact angle on droplet height. The term $P(e) - eP'(e)$ is plotted against e, as shown in Figure 27 [56].

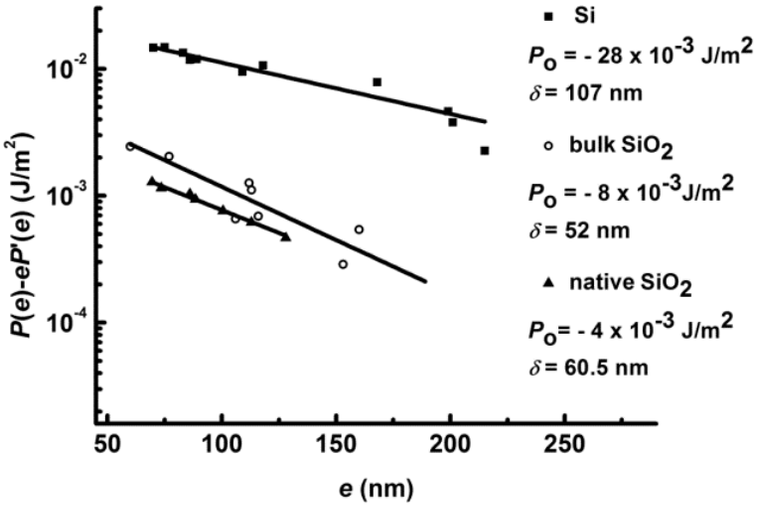

Figure 27. Semi-logarithmic scale plot of the term $P(e) - eP'(e)$ versus e

As the contact angle decreases with decreasing droplet height, an exponential distance dependence of the negative surface potential, $P(e) = P_0 \exp(-e/\delta)$, is expected to give a good fit of the data [52]. Here, P_0 and δ are the fitting parameters. From these parameters we determined the dependence of the potential energy on droplet height [56]:

http://dx.doi.org/10.5772/60886

$$P(e) = -28 \cdot 10^{-3} \exp(-e / 107\ \mathbf{nm})\ \mathbf{J/m^2}\ \textbf{for glycerol on silicon}$$

$$P(e) = -4 \cdot 10^{-3} \exp(-e / 60.5\ \mathbf{nm})\ \mathbf{J/m^2}\ \textbf{for glycerol on native SiO}_2$$

$$P(e) = -8 \cdot 10^{-3} \exp(-e / 52\ \mathbf{nm})\ \mathbf{J/m^2}\ \textbf{for glycerol on bulk SiO}_2$$

The strength of the potential at $e = 0$ nm gives the spreading coefficient S for each case [56]:

$$S = P(0) = -28 \cdot 10^{-3}\ \mathbf{J/m^2}\ \textbf{for glycerol on silicon}$$

$$S = P(0) = -4 \cdot 10^{-3}\ \mathbf{J/m^2}\ \textbf{for glycerol on native SiO}_2$$

$$S = P(0) = -8 \cdot 10^{-3}\ \mathbf{J/m^2}\ \textbf{for glycerol on bulk SiO}_2.$$

The (negative) values of the disjoining pressure Π, resulting from these potential energies, are: 2.8 atm, 0.6 atm, and 1.5 atm, for glycerol on silicon, native SiO_2, and bulk SiO_2, respectively.

Table 1 summarizes the results obtained in the studies described in Sections 4 a–c [54-56], for the parameters P_0, δ, and Π. In order to make a direct comparison with other experiments, in Table 1 are also introduced the results on mica, stainless steel, HOPG, and aluminum substrates, described in Sections 4 a and 4 b. In all these cases, the values of spreading coefficient indicate a weak hydrophobic interaction for the systems, compared to the surface tension of glycerol and sulfuric acid [54-56].

liquid / substrate	P_0 (mJ/m²)	δ (nm)	Π (atm)
glycerol / silicon	–28	107	2.8
glycerol / native SiO_2	–4	60.5	0.6
glycerol / bulk SiO_2	–8	52	1.5
glycerol / mica	–1.4	50	0.28
glycerol / stainless steel	–3.98	86	0.46
glycerol / HOPG	–6	150	0.4
glycerol / aluminum	–15	316	0.47
H_2SO_4 / HOPG	–13	10	13

Table 1. Values of P_0, δ, and Π for glycerol on silicon, native and bulk SiO_2, mica, stainless steel, HOPG and aluminum, and for H_2SO_4 on HOPG.

5.4. Conclusions

SPFM, one of the most advanced noncontact techniques having nanometer spatial resolution, was successfully used, together with suitable theoretical models, to determine the potential energy, disjoining pressure and spreading coefficient from the dependence of the contact angle on droplet height, for micro- and nanodroplets. The contact angle was directly measured from the recorded topography images of the droplets. The testing liquids were chosen for their suitable properties: sufficiently high boiling point (290°C for glycerol, 337°C for 98% wt. sulfuric acid, at atmospheric pressure) and low vapor pressure (0.26 mbar for glycerol at 100°C; 1.3 mbar for sulfuric acid at 145.8°C). These ensure a low enough evaporation rate of the micro- and nanodroplets during measurements. The tested materials (HOPG, mica, stainless steel, aluminum, silicon, and silicon dioxide) were chosen based on specific considerations: *i*) HOPG and mica, due to the ease with which they can be cleaved, can be regarded as model surfaces as they can be readily prepared in the form of defect free, atomically clean and flat surfaces; *ii*) stainless steel and aluminum because of their importance and widespread use in industrial applications, from precision mechanics to heavy construction machinery and structures; *iii*) silicon and silicon dioxide as key materials in the continuously growing fields of MEMS/NEMS and understanding their wetting behavior at micro- and nanoscale is a key factor in the design and optimization of these technologies. A large range of technologies, all of which play continuously growing roles in the development of current and innovative applications, from the silicon-based electronics industry to MEMS/NEMS manufacturing, as well as lab-on-chip devices or dip pen nanolithography, are fully benefiting from the qualitative and quantitative information about wetting properties at the micro- and nanoscale on silicon-based materials, offered by the SPFM technique described above.

6. General conclusions

Wetting properties at the macroscopic scale benefited from extensive studies during the course of the last two centuries. A lot of scientific literature has been dedicated to theoretical advancements towards the understanding of the involved mechanisms and physical quantities, and to the development of suitable experimental techniques.

The basic and advanced techniques used to characterize the wettability of materials at the macro-, micro-, and nanoscale have been described in this chapter. Due to the high demand of understanding the wetting and adhesion at micro-scale, new and innovative techniques for measuring the wettability of surfaces continue to emerge.

The interest for studying wetting properties at the micro- and nanoscale started increasing with the rapid development of micro- and nanotechnologies in the last decades. At these scales, local inhomogeneity of the materials plays a significant role in the behavior of liquids coming into contact with solid surfaces. The SPM family of techniques, which actually made possible the evolution of nanotechnology, offers direct methods for determining nanoscale adhesion and wetting properties. SPFM, as a truly noncontact technique of this family, stands out in particular by enabling the investigation of the topography of diverse liquid surfaces, thus proving to be extremely useful for the study of wetting properties at micro- and nanoscale. It

overcomes the difficulties inherent to "classical" AFM techniques (e.g., difficult to maintain stable feedback on liquid surfaces) and offers a direct means for the measurement of the microscopic contact angle. Nevertheless, the wetting behavior at the micro- and nanoscale is still an open field with many open questions related to wetting mechanisms and manipulation of micro- and nanodroplets.

Author details

Antoniu Moldovan[1,2] and Marius Enachescu[1*]

*Address all correspondence to: marius.enachescu@upb.ro

1 Center for Surface Science and Nanotechnology, University POLITEHNICA of Bucharest, Romania

2 National Institute for Laser, Plasma and Radiation Physics (INFLPR), Magurele – Bucharest, Romania

References

[1] Heo SY, Park BJ, Jeong JR, Yoon SG. Enhanced transmittance, mechanical durability, and anti-fingerprinting qualities of silver nanoparticles deposited onto glass substrates. Journal of Alloys and Compounds 2014; 602 255–260. DOI: 10.1016/j.jallcom.2014.03.019

[2] Kolattukudy PE. Natural waxes on fruits. Post Harvest Pomology Newsletter 1984; 2(2) 3–7

[3] Yuan Y, Randall Lee T. Contact angle and wetting properties. In: Bracco G, Holst B (ed.) Surface Science Techniques. Springer Series in Surface Science. Berlin, Heidelberg: Springer-Verlag 2013; 51 3–34. DOI: 10.1007/978-3-642-34243-1_1

[4] Méndez-Vilas A, Jódar-Reyes AB, González-Martín ML. Ultrasmall liquid droplets on solid surfaces: production, imaging, and relevance for current wetting research. Small 2009; 5(12) 1366–1390. DOI: 10.1002/smll.200800819

[5] Bush J. 18.357 Interfacial Phenomena, Fall 2010. (Massachusetts Institute of Technology: MIT OpenCourseWare), http://ocw.mit.edu (Accessed 17 Apr, 2015). License: Creative Commons BY-NC-SA

[6] Beebe DJ, Mensing GA, Walker GM. Physics and applications of microfluidics in biology. Annual Review of Biomedical Engineering 2002; 4 261–286. DOI: 10.1146/annurev.bioeng.4.112601.125916

[7] de Gans BJ, Duineveld PC, Schubert US. Inkjet printing of polymers: state of the art and future developments. Advanced Materials 2004; 16(3) 203–213. DOI: 10.1002/adma.200300385

[8] Bachofen H, Schürch S. Alveolar surface forces and lung architecture. Comparative Biochemistry and Physiology Part A: Molecular & Integrative Physiology 2001; 129(1) 183–193. DOI: 10.1016/S1095-6433(01)00315-4

[9] Hidalgo A, Cruz A, Pérez-Gil J. Barrier or carrier? Pulmonary surfactant and drug delivery. European Journal of Pharmaceutics and Biopharmaceutics 2015 (article in press). DOI: 10.1016/j.ejpb.2015.02.014

[10] Tabor D, Winterton RHS. The direct measurement of normal and retarded van der Waals forces. Proceedings of the Royal Society of London, A 1969; 312 435–450. DOI: 10.1098/rspa.1969.0169

[11] Israelachvili JN, Tabor D. The measurement of van der Waals dispersion forces in the range 1.5 to 130 nm. Proceedings of the Royal Society of London, A 1972; 331 19–38. DOI: 10.1098/rspa.1972.0162

[12] Israelachvili JN, Tabor D. Van der Waals forces: theory and experiment. Progress in Surface and Membrane Science 1973; 7 1–55. DOI:10.1016/B978-0-12-571807-3.50006-5

[13] Israelachvili JN. Intermolecular and Surface Forces. Burlington: Academic Press 1992

[14] Israelachvili JN, Min Y, Akbulut M, Alig A, Carver G, Greene W, Kristiansen K, Meyer E, Pesika N, Rosenberg K, Zeng H. Recent advances in the surface forces apparatus (SFA) technique. Reports on Progress in Physics 2010; 73 036601. DOI: 10.1088/0034-4885/73/3/036601

[15] Kristiansen K, McGuiggan P, Carver G, Meinhart C, Israelachvili JN. 3D force and displacement sensor for SFA and AFM measurements. Langmuir 2008; 24 1541–1549. DOI: 10.1021/la702380h

[16] Idziak SH, Safinya CR, Hill RS, Kraiser KE, Ruths M, Warriner HE, Steinberg S, Liang KS, Israelachvili JN. The x-ray surface forces apparatus—structure of a thin smectic liquid crystal film under confinement. Science 1994; 264 1915–1918. DOI: 10.1126/science.264.5167.1915

[17] Mukhopadhyay A, Zhao J, Chul Bae S, Granick S. An integrated platform for surface forces measurements and fluorescence correlation spectroscopy. Review of Scientific Instruments 2003; 74 3067–3072. DOI: 10.1063/1.1570947

[18] Joanny JF, de Gennes PG. A model for contact angle hysteresis. Journal of Chemical Physics. 1984; 81 552. DOI: 10.1063/1.447337

[19] Eral HB, 't Mannetje DJCM, Oh JM. Contact angle hysteresis: a review of fundamentals and applications. Colloid and Polymer Science 2013; 291 (2) 247. DOI: 10.1007/s00396-012-2796-6

[20] Gao L, McCarthy TJ. Contact angle hysteresis explained. Langmuir 2006; 22 (14) 6234–6237. DOI: 10.1021/la060254j

[21] Yazdanpanah MM, Hosseini M, Pabba S, Berry SM, Dobrokhotov VV, Safir A, Keynton RS, Cohn RW. Micro-Wilhelmy and related liquid property measurements using constant-diameter nanoneedle-tipped atomic force microscope probes. Langmuir 2008; 24 13753–13764. DOI: 10.1021/la802820u

[22] Bigelow WC, Pickett DL, Zisman WA. Oleophobic monolayers: I. Films adsorbed from solution in non-polar liquids. Journal of Colloid Science 1946; 1 513–538. DOI: 10.1016/0095-8522(46)90059-1

[23] Erbil HY, McHale G, Rowan SM, Newton MI. Determination of the receding contact angle of sessile drops on polymer surfaces by evaporation. Langmuir 1999; 15 7378–7385. DOI: 10.1021/la9900831

[24] Srinivasan S, McKinley GH, Cohen RE. Assessing the accuracy of contact angle measurements for sessile drops on liquid-repellent surfaces. Langmuir 2011; 27 13582–13589. DOI: 10.1021/la2031208

[25] Wan JM, Wilson JL. Colloid transport in unsaturated porous media. Water Resources Research 1994; 30 857–864. DOI: 10.1029/93WR03017

[26] Wu W. Baseline studies of The Clay Minerals Society source clays: colloid and surface phenomena. Clays and Clay Minerals 2001; 49 446–452

[27] Costanzo PM, Wu W, Giese RF, van Oss CJ. Comparison between direct contact angle measurements and thin layer wicking on synthetic monosized cuboid hematite particles. Langmuir 1995; 11 1827–1830. DOI: 10.1021/la00005a064

[28] Wan JM, Wilson JL, Kieft TL. Influence of the gas-water interface on transport of microorganisms through unsaturated porous media. Applied and Environmental Microbiology 1994; 60 509–516

[29] Abu-Lail NI, Camesano TA. The effect of solvent polarity on the molecular surface properties and adhesion of *Escherichia coli.* Colloids and Surfaces B: Biointerfaces 2006; 51 62–70. DOI: 10.1016/j.colsurfb.2006.05.009

[30] Kukavica-Ibrulj I, Darveau A, Jean J, Fliss I. Hepatitis A virus attachment to agri-food surfaces using immunological, virological and thermodynamic assays. Journal of Applied Microbiology 2004; 97 923–934. DOI: 10.1111/j.1365-2672.2004.02366.x

[31] Sundberg M, Månsson A, Tågerud S. Contact angle measurements by confocal microscopy for non-destructive microscale surface characterization. Journal of Colloid and Interface Science 2007; 313 454–460. DOI:10.1016/j.jcis.2007.04.067

[32] Fischer DG, Ovryn B. Interfacial shape and contact-angle measurement of transparent samples with confocal interference microscopy. Optics Letters 2000; 25 478–480. DOI: 10.1364/OL.25.000478

[33] Yu J, Wang H, Liu X. Direct measurement of macro contact angles through atomic force microscopy. International Journal of Heat and Mass Transfer 2013; 57 299–303. DOI: 10.1016/j.ijheatmasstransfer.2012.10.041

[34] Checco A, Guenoun P, Daillant J. Nonlinear dependence of the contact angle of nanodroplets on contact line curvature. Physical Review Letters 2003; 91 186101. DOI: 10.1103/PhysRevLett.91.186101

[35] Salmeron M. Nanoscale wetting and de-wetting of lubricants with scanning polarization force microscopy. In: Bhushan B (ed.) Fundamentals of Tribology and Bridging the Gap Between the Macro- and Micro/Nanoscales. NATO Science Series II. Dordrecht: Kluwer Academic Publishers 2001; 10 651–662

[36] Hu J, Xiao XD, Salmeron M. Scanning polarization force microscopy: a technique for imaging liquids and weakly adsorbed layers. Applied Physics Letters 1995; 67 476–478. DOI: 10.1063/1.114541

[37] Jung YC, Bhushan B. Technique to measure contact angle of micro/nanodroplets using atomic force microscopy. Journal of Vacuum Science and Technology A 2008; 26 777–782. DOI: 10.1116/1.2832409

[38] Hu J, Xiao XD, Ogletree DF, Salmeron M. Imaging the condensation and evaporation of molecularly thin films of water with nanometer resolution. Science 1995; 268 267–269. DOI: 10.1126/science.268.5208.267

[39] Xu L, Lio A, Hu J, Ogletree DF, Salmeron M. Wetting and capillary phenomena of water on mica. Journal of Physical Chemistry B 1998; 102 540–548. DOI: 10.1021/jp972289l

[40] Dai Q, Hu J, Salmeron M. Adsorption of water on NaCl (100) surfaces: role of atomic steps. Journal of Physical Chemistry B 1997; 101 1994–1998. DOI: 10.1021/jp9625772

[41] Luna M, Rieutord F, Melman NA, Dai Q, Salmeron M. Adsorption of water on alkali halide surfaces studied by scanning polarization force microscopy. Journal of Physical Chemistry A 1998; 102 6793–6800. DOI: 10.1021/jp9820875

[42] Dai Q, Hu J, Freedman A, Robinson GN, Salmeron M. Nanoscale imaging of a corrosion reaction: sulfuric acid droplets on aluminum surfaces. Journal of Physical Chemistry 1996; 100 9–11. DOI: 10.1021/jp952538a

[43] Rieutord F, Salmeron M. Wetting properties at the submicrometer scale: a scanning polarization force microscopy study. Journal of Physical Chemistry B 1998; 102 3941–3944. DOI: 10.1021/jp980149l

[44] Xu L, Salmeron M, Bardon S. Wetting and molecular orientation of 8CB on silicon substrates. Physical Review Letters 2000; 84 1519–1522. DOI: 10.1103/PhysRevLett.84.1519

[45] Xu L, Ogletree DF, Salmeron M, Tang H, Gui J, Marchon B. De-wetting of lubricants on hard disks. Journal of Chemical Physics 2000; 112 2952–2957. DOI: 10.1063/1.480868

[46] Dai Q, Vurens G, Luna M, Salmeron M. Lubricant distribution on hard disk surfaces: effect of humidity and terminal group reactivity. Langmuir 1997; 13 4401–4406. DOI: 10.1021/la970323h

[47] Reder-Christ K, Schmitz P, Bota M, Gerber U, Falkenstein-Paul H, Fuß C, Enachescu M, Bendas G. A dry membrane protection technique to allow surface acoustic wave biosensor measurements of biological model membrane approaches. Sensors 2013; 13 12392–12405. DOI: 10.3390/s130912392

[48] Calin M, Stan D, Schlesinger M, Simion V, Deleanu M, Ana Constantinescu C, Gan AM, Pirvulescu MM, Butoi E, Manduteanu I, Bota M, Enachescu M, Borsig L, Bendas G, Simionescu M. VCAM-1 directed target-sensitive liposomes carrying CCR2 antagonists bind to activated endothelium and reduce adhesion and transmigration of monocytes. European Journal of Pharmaceutics and Biopharmaceutics 2015; 89 18–29. DOI:10.1016/j.ejpb.2014.11.016

[49] Xu L, Salmeron M. Studies of wetting and capillary phenomena at nanometer scale with scanning polarization force microscopy. In: Rosoff M (ed.) Nano-Surface Chemistry. New York: Marcel Dekker 2001; ch. 6 243–287

[50] Martin Y, Abraham DW, Wickramasinghe HK. High-resolution capacitance measurement and potentiometry by force microscopy. Applied Physics Letters 1988; 52 1103–1105. DOI: 10.1063/1.99224

[51] de Gennes PG. Wetting: statics and dynamics. Reviews of Modern Physics 1985; 57 827–863. DOI: 10.1103/RevModPhys.57.827

[52] Xu L, Salmeron M. Scanning polarization force microscopy study of the condensation and wetting properties of glycerol on mica. Journal of Physical Chemistry B 1998; 102 7210–7215. DOI: 10.1021/jp981834v

[53] Derjaguin BNV, Churaev NV, Muller VM, Kitchener JA. Surface Forces. New York: Consultants Bureau 1987; ch. V

[54] Moldovan A, Bota M, Poteca TD, Boerasu I, Bojin D, Buzatu D, Enachescu M. Scanning polarization force microscopy investigation of contact angle and disjoining pressure of glycerol and sulfuric acid on highly oriented pyrolytic graphite and aluminum. European Physical Journal – Applied Physics 2013; 64 31302. DOI: 10.1051/epjap/2013130235

[55] Moldovan A, Bota M, Boerasu I, Dorobantu D, Bojin D, Buzatu D, Enachescu M. Wetting properties of glycerol on mica and stainless steel by scanning polarization force microscopy. Journal of Optoelectronics and Advanced Materials 2013; 15 1101–1105

[56] Moldovan A, Bota M, Dorobantu D, Boerasu I, Bojin D, Buzatu D, Enachescu M. Wetting properties of glycerol on silicon, native SiO_2, and bulk SiO_2 by scanning polarization force microscopy. Journal of Adhesion Science and Technology 2014; 28 1277–1287. DOI: 10.1080/01694243.2014.900907

IntechOpen